

Deep convolutional neural network for shape optimization using level-set approach

Wrik Mallik · Neil Farvolden · Rajeev K. Jaiman · Jasmin Jelovica

The date of receipt and acceptance should be inserted later

Abstract This article presents a reduced-order modeling methodology for shape optimization applications via deep convolutional neural networks (CNNs). The CNN provides a nonlinear mapping between the shapes and their associated attributes while conserving the equivariance of these attributes to the shape translations. To implicitly represent complex shapes via a CNN-applicable Cartesian structured grid, a level-set method is employed. The CNN-based reduced-order model (ROM) is constructed in a completely data-driven manner, and suited for non-intrusive applications. We demonstrate our complete ROM-based shape optimization on a gradient-based three-dimensional shape optimization problem to minimize the induced drag of a wing in potential flow. We show a satisfactory comparison between ROM-based optima for the aerodynamic coefficients compared to their counterparts obtained via a potential flow solver. The predicted behavior of our ROM-based global optima closely matches the theoretical predictions. We also present the learning mechanism of the deep CNN model in a physically interpretable manner. The CNN-ROM-based shape optimization algorithm exhibits significant computational efficiency compared to full order model-based online optimization applications. Thus, it promises a tractable solution for shape optimization of complex configuration and physical problems.

Keywords Convolutional neural networks · Level-set method · Shape optimization

Wrik Mallik
Rajeev K. Jaiman
Jasmin Jelovica

Department of Mechanical Engineering,
The University of British Columbia, Vancouver, BC, Canada

Neil Farvolden

Institute for Aerospace Studies,
University of Toronto, Toronto, ON, Canada

1 Introduction

Shape optimization has gained considerable interest over the last three-four decades with the advent of high-performance computing resources and the increasing popularity of numerical solution techniques such as the finite element method (FEM), finite difference method (FDM), and among others. In structural optimization, optimizing structural boundaries can often prove more efficient in structural weight reduction than optimizing structural thickness [13]. Thus, shape optimization has grown in popularity over sizing optimization, especially with advanced high performance computing facilities. Similarly, on the side of fluid mechanics, the large effect of changes in airfoil shapes on their drag and aerodynamic performance has been known to the aerospace community for several decades. Thus, with the advent of computational fluid dynamics (CFD) simulations that can predict accurate flow solutions, there has been a growing interest in aerodynamic shape optimization over the last two decades [36, 38].

Integrating high-fidelity computational structural mechanics (CSM) or CFD simulations within an optimization algorithm is often restricted by the huge computational expense of these simulations. This has restricted the community what computational model complexity can be realistically employed in an optimization study. Some recent fluid dynamic shape optimization studies with high-fidelity CFD-based analyses [11, 24, 15] have been conducted. These studies have completely relied on a gradient-based search algorithm, which can very frequently converge to local optima for a non-convex, multi-objective shape optimization problem, especially when there are many design parameters [7, 44]. However, employing expensive metaheuristic algorithms which can empirically converge to global optima remain largely non-tractable with high-fidelity solvers. This has motivated the present-day researchers in the development of computationally efficient reduced-order models (ROMs)/surrogate models, which can accurately emulate the computationally expensive full-order models (FOM) during the online application.

A variety of data-driven reduced-order modeling techniques exist in literature like Kriging [22] (also known as Gaussian process regression) and its variants [39, 4], polynomial chaos expansions [2], and support vector machines [10]. Some reviews have elaborated the applications of these methods for shape optimization applications [21, 14, 52]. Of all these methods, Kriging is the most widely used method in various engineering analysis and design tasks [47, 9, 26]. However, Kriging suffers from a variety of issues such as being poor at approximating discontinuous functions [35], difficulty in handling high-dimensional problems [34], costly to use in the presence of a large number of data samples [19], and being difficult to implement for solving certain inverse problems with strong nonlinearities [3].

With the advent of deep learning (DL), neural networks (NNs) have been demonstrated as an effective approximation technique for most general complex functions [8, 16]. They do not suffer from the many limitations of Kriging mentioned above and are replacing Kriging as the best ROM candidates for optimization applications [5, 33]. Besides, increasingly wide feed-forward NNs (also called multi-layer perceptrons (MLPs)), have been demonstrated to converge to Gaussian processes under broad conditions [29]. This has led to the increased applications of MLPs [18, 41, 49] and gradient-enhanced MLPs [5] for ROM-based shape optimization studies.

In this article, we present an efficient and unique approach for developing data-driven ROMs for shape optimization applications. We employ convolutional neural networks (CNNs) [12] as a ROM for the higher-order computational model. CNNs have demonstrated excellent image learning capability in the commercial DL community because of the shared memory employed during the learning. The convolution (or cross-correlation) operation along the shared memory parameters endows CNNs with translational equivariance, whereby they can learn how the features of the input transform due to a translation of the input itself. Two or three-dimensional shapes can easily be pictured as pixels or voxels, respectively. Similarly, aerodynamic force coefficients, structural stresses, etc., associated with such shapes can be considered as output features of these pixels/voxels, and can thus be efficiently learned via CNNs. This is our motivation for employing CNNs as a ROM to learn the accurate mapping between the shapes and their associated features arising from various physical phenomena. A detailed discussion on how the convolution operation and translation equivariance forms strong geometric priors to enhance the learning capacity over MLPs is presented in Ref. [12].

Level-set methods can provide an implicit representation of even complex shapes on a fixed Cartesian grid. Often such an implicit representation leads to a coarse-grained representation of shapes which would otherwise require a very fine mesh for explicit representation [40]. This has often motivated the application of various forms of level-set representation approach for shape [1, 48] and topology optimization [50, 48]. Although this remains one of the reasons for the application of level-set methods for the present article, the primary reason is somewhat different. Here we are employing CNNs as our DL model. CNNs require input data in the form of a uniform point cloud on a Euclidean domain. Thus, the level-set representation of shapes on a relatively coarse, uniform Cartesian grid provides input information in a form directly employable by CNNs. Such features of level-set representation were employed for generating CNN input data in a previous study for learning the aerodynamic force coefficients obtained from Navier-Stokes simulations of the two-dimensional flow around bluff-bodies was presented in the past [30]. Here we employ it for the first time for implicit shape representation on a CNN employable grid to develop a ROM for shape optimization applications.

In the present study, we specifically employ deep CNNs with level-set shape representations to obtain a mapping between three-dimensional wing configurations and their aerodynamic force coefficients. The FOM employed here is a potential flow solver, which can predict the lift and induced drag generated by the wing at low speeds. However, it could easily be replaced by higher-fidelity CFD simulations or experiments without any loss of generality, as the CNN-based mapping is completely data-driven. The FOM is employed for generating an adequate number of input and output data sets to train the deep CNN model. The CNN-based ROM is subsequently employed for non-intrusive shape optimization of a wing shape to minimize the wing's drag coefficient, while prescribed constraints are applied on the wing lift coefficient and minimum thickness ratio.

The methodology of developing the CNN-based ROM with level-set methods, its application in the constrained optimization study, and the accuracy of the results predicted by the CNN model are discussed in the paper. We specifically demonstrate the optimization applications with gradient-based methods but the non-intrusive application enables seamless integration with other gradient-free optimization algorithms like trust region-based methods [27] and genetic algorithms

[37]. We also explore the feature space of various convolution layers of the deep CNN model to provide interpretability to the deep CNN's learning mechanism. The computational efficiency of the present approach compared to FOM-based shape optimization is also discussed. Such application of deep CNNs with level-set methods as ROMs for shape optimization is presented here for the first time.

2 Uniqueness of the proposed reduced-order modeling approach

There has been a recent application of NNs as ROMs for shape optimization applications [5, 33]. These articles have focused on MLPs as their DL framework and have specifically employed a gradient-enhanced version of such networks. While such methods have shown good accuracy, they have been explicitly developed for gradient-based optimization algorithms, which may not be adequate in many cases [7, 44]. Another set of data-driven ROMs employed recently was based on proper orthogonal decomposition (POD) bases [51] and hyper-reduction based on POD modes [27]. While the latter method was developed for a non-intrusive application, linear projection methods like POD are less efficient for certain convection-dominated fluid mechanics problems [32].

Our proposed model order reduction approach is unique to such recent articles in the following ways:

- We employ CNNs as our DL model, which is significantly more efficient than linear projection-based model reduction approaches for even the most complex physical cases [32].
- We employ CNNs to obtain a map between shapes represented on a uniform Cartesian grid and their associated attributes. CNNs are specifically suited for such learning tasks aided by certain geometric priors. These are discussed later in the article.
- We employ level-set methods for implicit shape representation, which allows us to represent shape information on a CNN-employable grid. Furthermore, such implicit representation can be obtained on a coarser mesh with fewer parameters compared to explicit representation with free-form-deformation parameters employed for three-dimensional shape optimization study [38, 11].

3 Deep learning-based model order reduction methodology

The DL-based model order reduction methodology consists of two parts, the implicit shape representation, and the development of the DL model for learning the functional relation between shapes and their associated attributes. These are explained below in detail.

3.1 CNN: a geometric DL model

Successfully learning the changes in attributes associated with two or three-dimensional shapes as the shapes change themselves, requires the DL model to satisfy certain prior geometric assumptions. CNNs can satisfy these geometric priors either directly or approximately, resulting in tremendous success for similar applications in

the field of computer vision [23]. These geometric priors required for the supervised learning task are discussed below.

Let us consider a compact d -dimensional Euclidean domain $\Omega = [0, 1]^d \subset \mathbb{R}^d$ on which square integrable functions $f \in L^2(\Omega)$ are defined. We consider a generic supervised learning environment for obtaining an unknown function $y : L^2(\Omega) \rightarrow \mathcal{Y}$ on a training set,

$$\{f_i \in L^2(\Omega), y_i = y(f_i)\}_{i \in \mathcal{I}}. \quad (1)$$

We are interested in regression tasks, thus $\mathcal{Y} = \mathbb{R}^m$. For the proposed learning problem, the unknown function y needs to satisfy the crucial prior assumptions explained below.

Stationarity: Our first assumption is that depending on the task, the function y is either invariant or equivariant with respect to translations. Here

$$\mathcal{T}_v f(x) = f((x - v)), \quad x, v \in \Omega, \quad (2)$$

is defined as a translation operator acting on functions $f \in L^2(\Omega)$. When we consider translation invariance, we have $y(\mathcal{T}_v f) = y(f)$ for any $f \in L^2(\Omega)$ and $v \in \Omega$. For translational equivariance, we have $y(\mathcal{T}_v f) = \mathcal{T}_v y(f)$.

Local deformations and scale separation: We also desire y to be stable to local deformations \mathcal{L}_τ , where $\tau : \Omega \rightarrow \Omega$ is a smooth vector field, acts on $L^2(\Omega)$ as $\mathcal{L}_\tau f(x) = f(x - \tau(x))$.

We briefly explain below how the CNN satisfies such prior assumptions during the forward propagation phase of the supervised learning algorithm. The supervised learning algorithm also includes a backpropagation phases, which ensures the CNN framework learns optimal parameters to minimize a prescribed loss function.

3.1.1 Forward propagation phase

In the present application, stationarity and stability to local translations are both leveraged in the CNN framework as follows. The CNN network consists of several convolutional layers of the form $C(\mathbf{f})$ which sequentially performs a set of convolution operation of the form $\mathbf{g} = \kappa_A(\mathbf{f})$, a batch-normalization operation β , and a point-wise non-linearity ξ , acting on a p -dimensional input $\mathbf{f}(x) = (f_1(x), \dots, f_p(x))$,

$$C(\mathbf{f}) = \xi(\beta(\kappa_A(\mathbf{f}))). \quad (3)$$

The convolution operation $\kappa_\Gamma(\mathbf{f})$ operates by applying a set of kernels (or filters) $A = (\lambda_{l,l'})$, $l = 1, \dots, p, l' = 1, \dots, p$,

$$g_l(x) = \sum_{l'=1}^p (f_{l'} * \lambda_{l,l'})(x), \quad (4)$$

producing a q -dimensional output $\mathbf{g}(x) = (g_1(x), \dots, g_q(x))$, often referred to as the feature maps. Here,

$$(f_{l'} * \lambda)(x) = \int_{\Omega} f(x - x') \lambda(x') dx', \quad (5)$$

denotes a standard convolution operation.

Batch normalization is an operation used to stabilize the training process and ensure faster training convergence by normalizing the output \mathbf{g} of a convolution operation by their mean μ and variance σ ,

$$\beta(\mathbf{g}) = \frac{\mathbf{g} - \mu}{\sqrt{\sigma + \epsilon}}, \quad (6)$$

where ϵ is a small positive value used to improve numerical stability when $\sigma \rightarrow 0$. Further details of the batch normalization process can be obtained in Ref. [17]. Finally, we introduce nonlinearity in our learning mechanism with a leaky rectified linear unit (leakyReLU) [25]. This is performed via the nonlinear activation layer as follows,

$$\xi(x) = \max(x, \gamma x), \quad (7)$$

where γ is a scaling factor.

A CNN model composed of K convolutional layers put together has a general hierarchical representation,

$$U_{\Theta}(\mathbf{f}) = (C_{(K)} \circ \dots \circ C_{(2)} \circ C_{(1)}), \quad (8)$$

where $\Theta = \{\Lambda^{(1)}, \dots, \Lambda^{(K)}\}$ is the set of all network parameters (all the kernel coefficients). The model is considered deep when the number of convolutional layers are large in number. Further details about the CNNs and their geometric learning capability on an Euclidean domain can be obtained in Ref. [6].

The deep CNN framework employed in this study consisted of four convolutional layers is illustrated in Fig. 1. The input data is the level-set representation, Φ , of the distance from the shape boundary. It is discussed next. The convolutional layers are followed by a fully connected layer to ensure a consistent dimension of the CNN output.

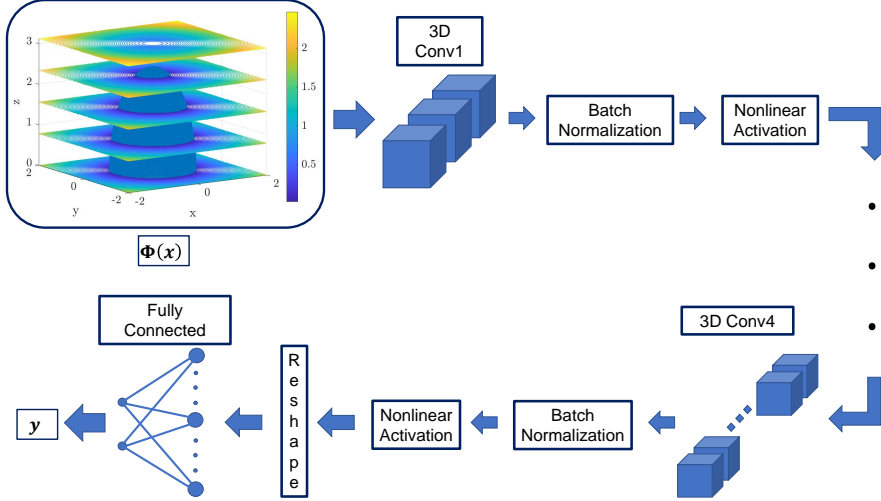


Fig. 1: Deep CNN architecture

3.1.2 Backpropagation phase

The role of backpropagation is to compute the errors between the target, \mathbf{y} , and the predicted output, $\hat{\mathbf{y}}$, and update the trainable network parameters to minimize the errors. The target \mathbf{y} is obtained from the FOM for the given inputs. The errors are computed via a loss function computing mean square error over a batch size n_b ,

$$\mathcal{L}(\hat{\mathbf{y}}, \mathbf{y}) = \frac{1}{2} \sum_{i=1}^{n_b} (\hat{\mathbf{y}}_i - \mathbf{y}_i)^2. \quad (9)$$

The weights and biases of the convolutional kernels and the fully connected layer are denoted generally as W and b from the trainable network parameters. These are updated iteratively via the gradient descent-based optimization Adam [20]. Adam is run over several iterations to achieve convergence. To accelerate the convergence, the input dataset is divided into several mini-batches, and the loss function is evaluated for each mini-batch. The order of the mini-batches is selected randomly leading to a stochastic optimization process.

The weight (and similarly the bias) update process is shown below

$$W^{t+1} = W^t - \frac{\alpha u^t}{\sqrt{v^t} + \epsilon}, \quad (10)$$

where α is the initial learning rate, u_w^t is an adaptive gradient of the loss with respect to the weight, and v_w^t is a moving average of the element-wise squares of the loss gradients. The superscript t denotes the iteration of the optimization process. Here, we consider α as a hyperparameter than can be tuned to improve the network's predictions. u_w^t and v_w^t are obtained as,

$$\begin{aligned} u_w^t &= \beta_1 u^{t-1} + (1 - \beta_1) \frac{\partial \mathcal{L}}{\partial W} \\ v_w^t &= \beta_2 v^{t-1} + (1 - \beta_2) \left(\frac{\partial \mathcal{L}}{\partial W} \right)^2. \end{aligned} \quad (11)$$

The adaptive gradient u_w^t helps to reduce the oscillations of the stochastic optimizer as it converges to an optimum by reducing the step size along the path of the steepest gradient. v_w^t serves a similar purpose but instead adaptively decays the learning rate of the weight update with increasing iterations, as the optimizer converges to the optimal weights. β_1 and β_2 are the decay factor of the gradients and squared gradients of the loss and epsilon is a stabilizer of the numerical process for very small values of v_w^t .

3.2 Level-set method for shape representation

Here we employ a level-set method to represent the three-dimensional shape on a structured three-dimensional Cartesian grid. Level-set methods are well-known for their capacity to implicitly represent even complex shapes on a coarser mesh [40] compared to explicit techniques like free-form deformation variables. The computational efficiency of such coarse-grained, implicit representation has motivated their extensive application for shape and topology optimization studies [1, 50, 48].

We represent the three-dimensional shape via level-sets of the minimum Euclidean distance of any point on the level-set grid from the shape boundary. The boundary and domain inside it are represented by zero level-sets. These are formulated as follows,

$$\Phi(\mathbf{x}; \Gamma) = \begin{cases} \min(\|\mathbf{x} - \mathbf{x}_\Gamma\|_2), & \forall \mathbf{x} \in \Omega \\ 0 & \forall \mathbf{x} \in \Gamma, \\ 0 & \forall \mathbf{x} \in D \end{cases} \quad (12)$$

where \mathbf{x} represents the Cartesian coordinates, Γ represents the shape boundary, Ω represents the domain outside the boundary, and D represents the domain inside the boundary Γ . Slices of the various level-set iso-surfaces drawn at various locations along the z -axis are shown in Fig. 2 for an arbitrary ellipsoid configuration.

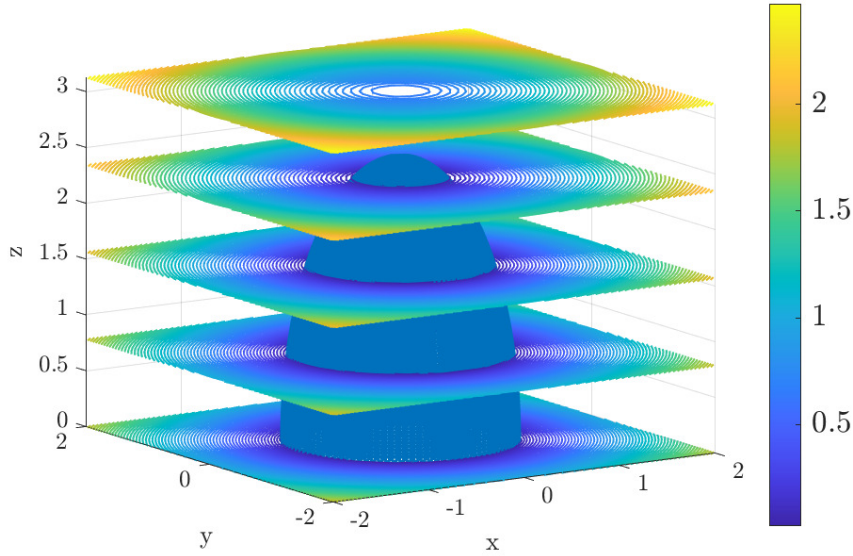


Fig. 2: Level-set distance functions representing a general ellipsoid structure

Apart from the implicit shape representation, the level-set method serves another purpose for the present application. Here we intend to employ CNNs as our DL model for the supervised learning of how physical attributes associated with various shapes change with their geometry. The CNNs learn such maps on a Euclidean domain and require a point cloud of the input data on a uniform, structured grid. The level-sets of distance function obtained on a uniform Cartesian grid thus provide our shape input in a form directly employable by CNNs.

4 DL-ROM-based shape optimization methodology

The DL-ROM-based shape optimization methodology can be divided into an optimization phase where the DL-ROM is applied in a non-intrusive manner to search the optima and a DL-ROM operation phase where the level-set shape representation and CNN prediction are carried out as a "black-box" with respect to the optimization algorithm. Fig. 3 shows a schematic demonstrating the flow of information in the shape optimization process. Interchange of information takes place at two stages, once when the design variables selected by the optimization algorithm are passed to the DL-ROM, and again when the shape attributes associated with these design variables are passed back to the optimization phase by the DL-ROM model. The DL-ROM is employed in a non-intrusive manner. A detailed explanation of the two phases of the complete DL-ROM-based shape optimization methodology is provided below.

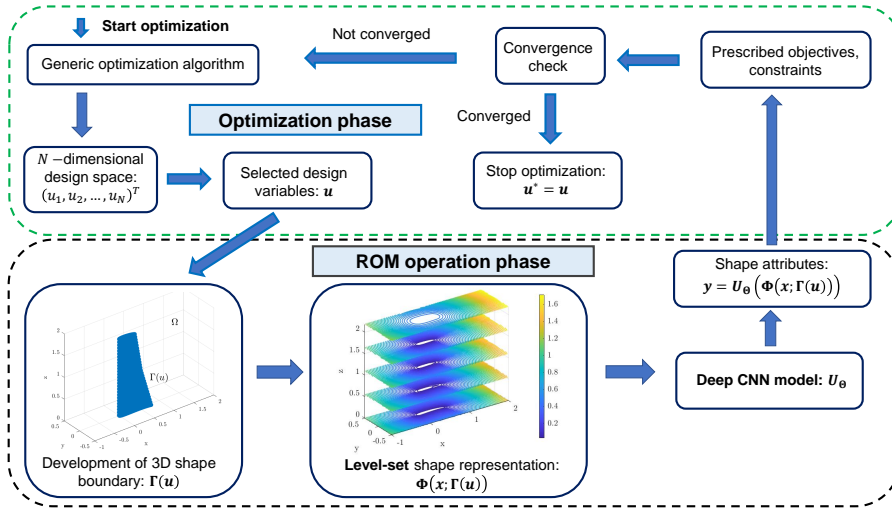


Fig. 3: DL-ROM-based shape optimization framework

4.1 Non-intrusive optimization phase

The shape optimization problem is formulated as,

$$\begin{aligned}
 & \underset{\mathbf{u} \in \mathcal{V}}{\text{minimize}} && \mathcal{J}(\mathbf{y}(\mathbf{u}), \mathbf{u}) \\
 & \text{subject to} && \mathcal{C}_{\mathcal{E}}(\mathbf{y}(\mathbf{u}), \mathbf{u}) = 0, \\
 & && \mathcal{C}_{\mathcal{I}}(\mathbf{y}(\mathbf{u}), \mathbf{u}) \leq 0.
 \end{aligned} \tag{13}$$

Here, \mathbf{u} are a set of N design variables, $\mathbf{u} = (u_1, u_2, \dots, u_N)$, $\mathbf{u} \in \mathbb{R}$, which can change the three-dimensional shapes. $\mathbf{y}(\mathbf{u})$ are the attributes of the shapes thus created and are obtained directly from \mathbf{u} via the black-box DL-ROM (Eq. 19)

during the DL-ROM operation phase, \mathcal{J} is the objective function, $\mathcal{C}_{\mathcal{E}}$ is the equality constraint and $\mathcal{C}_{\mathcal{I}}$ is the inequality constraint. $\mathcal{V} \subset \mathbb{R}^N$ represents the N -dimensional parameter space of all possible combination of design variables.

Eligible solutions to this problem are the ones that satisfy all constraints and are members of feasible set \mathbf{U}

$$\mathbf{U} = \{\varphi \left([u_1, \dots, u_N]^T \right) | \mathbf{b}_l \leq \mathbf{u} \leq \mathbf{b}_u\}, \quad (14)$$

which contains all variable permutations φ of \mathbf{x} between their lower and upper bounds, \mathbf{b}_l and \mathbf{b}_u , respectively. Thus, it contains all possible design alternatives.

The DL-ROM-based shape optimization methodology presented above is a generic formulation for non-intrusive DL-ROM applications, compatible with any generic optimization algorithm. In the present study, we employ a gradient-based algorithm to obtain our optimal configuration. The gradient of the objective function is computed as

$$\frac{d\mathcal{J}}{d\mathbf{u}} = \frac{\partial \mathcal{J}}{\partial \mathbf{u}} + \frac{\partial \mathcal{J}}{\partial \mathbf{y}} \frac{d\mathbf{y}}{d\mathbf{u}}, \quad (15)$$

where $\frac{\partial \mathcal{J}}{\partial \mathbf{u}}$ and $\frac{d\mathbf{y}}{d\mathbf{u}}$ are computed directly via any routine numerical differentiation scheme. The shape sensitivities of the constraints, $\frac{d\mathcal{C}_{\mathcal{E}}}{d\mathbf{u}}$ and $\frac{d\mathcal{C}_{\mathcal{I}}}{d\mathbf{u}}$, are computed numerically analogous to the shape sensitivity of the objective function. Such computation of sensitivities are termed as monolithic differentiation in the gradient-based shape optimization literature [28], and is employed when the computational model is treated as a "black-box" model.

4.2 DL-ROM operation phase

The DL-ROM operation phase is shown schematically in Fig. 3. Mathematically the DL-ROM operation during an online application can be formulated as follows. We have defined a set of design variables \mathbf{u} during the optimization phase used for creating a new three-dimensional configuration, and consequently change the boundary Γ of the shape. Thus, for optimization applications

$$\Gamma \equiv \Gamma(\mathbf{u}). \quad (16)$$

We can substitute Eq. 16 in Eq. 12 for optimization applications to obtain a design variable-based level-set representation,

$$\Phi(\mathbf{x}; \Gamma(\mathbf{u})) = \begin{cases} \min(\|\mathbf{x} - \mathbf{x}_{\Gamma(\mathbf{u})}\|_2), & \forall \mathbf{x} \in \Omega \\ 0, & \forall \mathbf{x} \in \Gamma(\mathbf{u}) \\ 0, & \forall \mathbf{x} \in D \end{cases} \quad (17)$$

We subsequently provide $\Phi(\mathbf{x}; \Gamma(\mathbf{u}))$ as inputs to the CNN model (Eq. 8) to obtain the shape attributes \mathbf{y} ,

$$\mathbf{y} = U_{\Theta}(\Phi(\mathbf{x}; \Gamma(\mathbf{u}))). \quad (18)$$

For non-intrusive application in an optimization algorithm, the DL-ROM presented in Eq. 18 can be substituted by a black-box idealization,

$$\mathbf{y} = \mathcal{F}(\mathbf{u}). \quad (19)$$

These shape attributes \mathbf{y} are now fed back into the optimization phase for computational of the objective function and constraint values, and their sensitivities with respect to the design variables \mathbf{u} if a gradient-based optimization algorithm is employed.

5 Test problem

Here we apply our CNN-based DL-ROM for shape optimization of a three-dimensional wing. Our objective is to minimize the induced drag of the wing $C_{D_i}(u)$, subject to certain constraints, all of which are functions of the design variables u . To perform a non-intrusive gradient-based shape optimization, we first begin with our offline training phase where the CNN is trained with an adequate number of wing shapes and associated force coefficients, as the input and output data sets, respectively. Here, the level-set methods are used to obtain the CNN input data for the wing shape on a structured Cartesian grid. A potential flow solver is employed to obtain the force coefficients for the wing configurations. After the training, we perform the DL-ROM-based non-intrusive optimization with a gradient-based algorithm according to the methodology as outlined in Fig. 3. Details of each of the various operations carried out at various phases of the whole methodology are provided as follows.

5.1 Parameterization of aerodynamic shape

In the current study, the wing shape is obtained by linearly interpolating the airfoils at the four sections along the span. These include the wing root and the tip sections and two other equally spaced intermediate sections. The airfoil shapes are formed by combining two Ferguson splines, one each for the top and bottom surfaces [42, 43]. Ferguson airfoils facilitate a relatively simple parameterization of the wing shape and yet enable the generation of a range of subsonic airfoils. Each of the wing sectional airfoils can be defined by eight shape variables. Amongst these, six variables satisfy the tangency and airfoil wedge angle constraints [42, 43], while the seventh and eighth variables define the sectional twist and airfoil chord, respectively. Thus, the four sections combine to form thirty-two design variables. The thirty-third and final design variable of the design variable set \mathbf{u} is the angle of incidence of the whole wing.

5.2 Aerodynamic analysis

The aerodynamic analysis for all three-dimensional wing configurations was conducted using linear lifting line theory (LLT) to provide a relatively quick generation of training data. Since we will consider low-speed flow at attached flow conditions, lifting line theory can provide a fairly accurate solution for the induced drag, C_{D_i} . Furthermore, most wing configurations selected here will be relatively thin. Under such conditions, the induced drag is the major contributor to the total drag on a wing, and LLT can be considered an acceptable FOM to obtain CNN training data. It is important to note that the DL-ROM is completely data-driven. Thus,

CNN prediction capabilities will not be affected if higher fidelity CFD or experimental data were augmented to the training dataset. Thus, we can use the present data generation approach to demonstrate the DL-ROM capabilities of the CNN without any loss of generality.

5.3 Level-set wing representation as CNN input

As explained earlier the level-sets of the distance function are computed on a three-dimensional Cartesian grid to be provided as input data to the CNN. Thus, the level-sets provide a discrete three-dimensional representation $\Phi \in \mathbb{R}^{m \times n \times p}$, where m , n and p represent the discretization dimensions in the x , y and z directions. As shown earlier in Eq. 17, the level-sets provide the Euclidean distance to the level-set grid point from the nearest point on the wing boundary, for all points external to the boundary.

The discrete wing distance level-set are computed on the bounded domain Ω ,

$$\Omega(x, y, z) \in \{[-1, 3] \times [0, 2] \times [-0.5, 0.5]\}, \quad (20)$$

along the x , y , and z directions, respectively. Following aerodynamic conventions, these represent the chord-wise, span-wise, and transverse directions. For the present test problem we had $m = 48$, $n = 16$ and $p = 32$. Higher resolutions were chosen for the x and z directions because of the more pronounced variability in the geometry along these axes. In the y direction, most of the axial variability in geometry comes from gradual changes in thickness and chord, and so the computational cost related to input size may be reduced without significant losses in model fidelity. In addition, the wing surface Γ is discretized using 50 chord-wise reference points (for each the top and bottom surface) and 50 span-wise reference points for computation of the Euclidean distance from the surface. This wing surface definition is independent of the wing level-set grid resolution.

5.4 Wing shape optimization problem

Our objective is to minimum the induce drag coefficient C_{D_i} subject to constraints on the design lift coefficient C_L , and the wing's minimum thickness ratio, t_c , by changing the wing's shape design variables \mathbf{u} . Thus, referring to the general non-intrusive shape optimization formulation presented in Eq. 13, for the present case,

$$\begin{aligned} \mathcal{J} &= C_{D_i}(\mathbf{u}) \\ \mathcal{C}_{\mathcal{I}}(1) &= t_c^* - \max(t_c(\mathbf{u})) \\ \mathcal{C}_{\mathcal{I}}(2) &= |C_L^* - C_L(\mathbf{u})| - \epsilon. \end{aligned} \quad (21)$$

There are no equality constraints for the present case of wing shape optimization.

The first constraint is applied on thickness ratio t_c to ensure that the maximum thickness ratio at all sections of the wing satisfies the minimum thickness, t_c^* . It is employed to obtain realistic manufacturing sizes and also indirectly ensure that the wing sections will be able to satisfy the stress requirements of a post-optimization structural analysis. The second constraint is applied on the lift coefficient C_L to ensure that it lies within a tolerance level, ϵ , of the design lift-coefficient C_L^* .

This ensures that the designs meet the required level-flight design lift conditions. For our study the minimum thickness ratio t_c^* is selected as 8% and the design lift-coefficient $C_L^* = 0.42$. We generally select the tolerance $\epsilon = 0.05C_L$.

6 Results

We first obtain our training data sets via FOM computations. These data are used for training, validation and testing our deep CNN model. We then analyze the feature space of the various composite convolutional layers of our deep CNN framework to provide interpretability to the learning mechanism of the CNN. We subsequently employ our CNN-based DL-ROM with the level-set shape representation for online applications with a gradient-based optimization algorithm. Each of these processes is detailed below.

6.1 CNN training data generation

To obtain the CNN training data sets, the level-set of the inputs must be first generated for a wide range of wing shape variables. The bounds for Ferguson airfoil geometry variables were selected as per the recommendations of Sobester and Forrester [43]. The wing incident angle of attack lower and upper bounds were selected as -3 and 10 degrees, respectively. This ensures a sufficiently wide range of lift and coefficient values for the CNN to accurately learn the forward map from the geometry parameters to the geometry features.

A Latin Hypercube (LH) sampling of the thirty-three dimension design variable space was performed to generate 17,500 wing configurations. Amongst them 15,000 were selected for the training set, 1,500 designs were selected for the validation set, and the remaining 1,000 designs were selected for the test set. The training, validation and test sets were also selected randomly from the total data sets. Furthermore, the mean and variance of each individual data set were inspected to ensure that they represent similar random distributions. The LLT was employed to obtain the C_L and C_D for all these designs and the distance function level sets were also computed. The distance function level-sets and the aerodynamic force coefficients form the input and output data sets for the CNN.

6.2 Training, validation and testing of the CNN

The CNN was trained on a single NVIDIA V100 Tensor Core GPU. Matlab's deep learning toolbox [45] was employed to develop and train the CNN architecture. Separate CNN models were employed for predicting C_L and C_{D_i} . The training convergence for both the C_L and C_{D_i} CNNs are presented in Fig. 4. It is observed that over four orders of mini-batch mean square error loss could be reduced by training the CNN for 60,000 iterations. The figure also shows that after about 50,000 iterations the loss reduction slows down considerably indicating convergence of the CNN model after 60,000 iterations.

The CNN predictions for the training and validation sets are presented in Figs. 5 (a) and (b), for C_L and C_{D_i} , respectively. For the lift coefficient, the

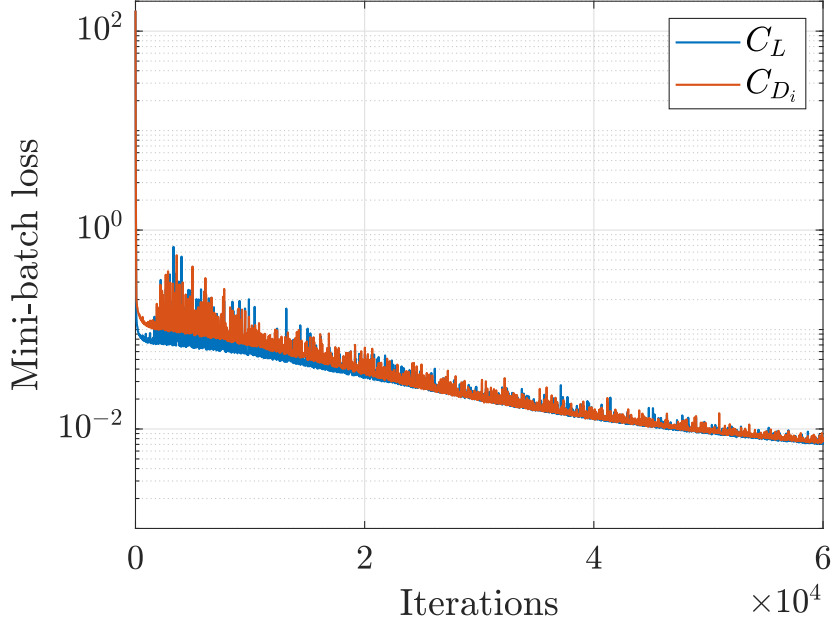
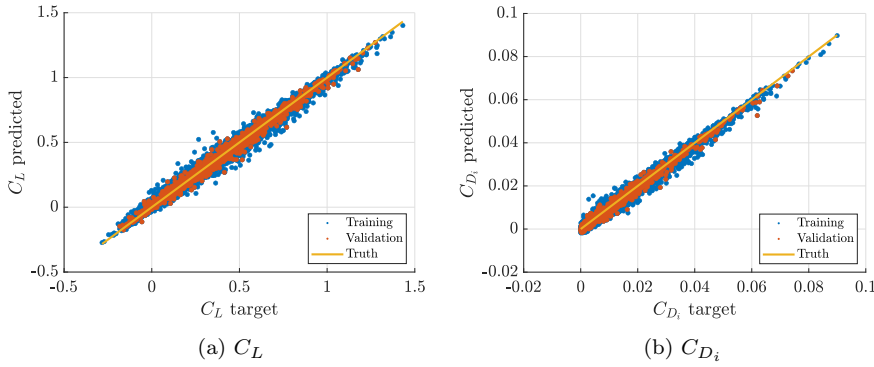


Fig. 4: Training convergence

training and validation predictions had $R^2 = 0.99$ and $R^2 = 0.98$, respectively. For the induced drag coefficients, the CNN predictions for the training and validation sets were $R^2 = 0.984$ and $R^2 = 0.975$, respectively.

Fig. 5: CNN predictions for C_L and C_{D_i}

Several of the hyperparameters of the CNN model was tuned to ensure the fastest training convergence and accurate generalization on the validation set. These include the number of convolutional layers, the size of the convolutional

kernels δ , and the number of convolutional kernels n_k . These hyperparameters mainly affect the CNN model size and generalizable capacity. The other hyperparameters include the initial training rate, decay of the training rate, and total training iterations. These hyperparameters affect the training convergence. We only show the sensitivity of the CNN models to a few of the key hyperparameters here for brevity.

First, we discuss the effect of the CNN model size (or the number of trainable parameters) on its predictive capability. We fix the number of convolutional layers as 4 and the kernel size δ in each layer. n_k is varied in each layer such that the total number of kernels in the deep CNN changes and this changes the CNN model size. It can be observed from Fig. 6 that on increasing the total number of kernels, the CNN’s training and validation prediction accuracy kept improving, for both the C_L and C_{D_i} , as indicated by their R^2 values. Validation and training prediction accuracy increased proportionally indicating that satisfactory training on 15,000 training sets usually assures reasonably generalizable prediction capability for other designs in the same parameter space. The network with around 50 total kernels was selected as the optimal one as increasing the number of parameters to 56 resulted in a 30% higher training cost with a very small improvement in prediction accuracy. The n_k distribution in each layer of the CNN for all the models shown in Fig. 6 is provided in Table 2 in the Appendix.

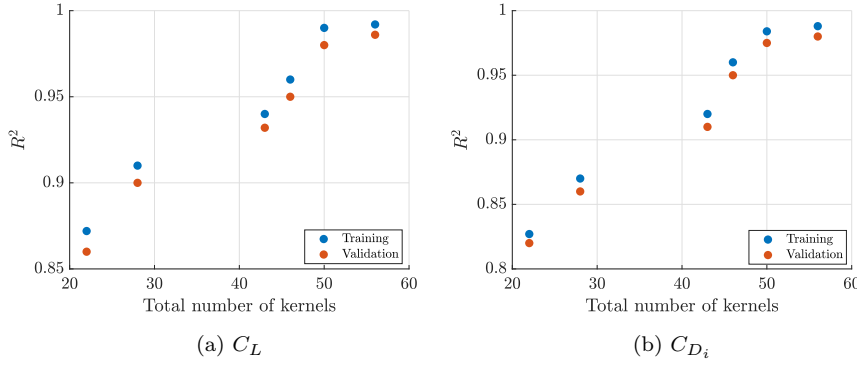


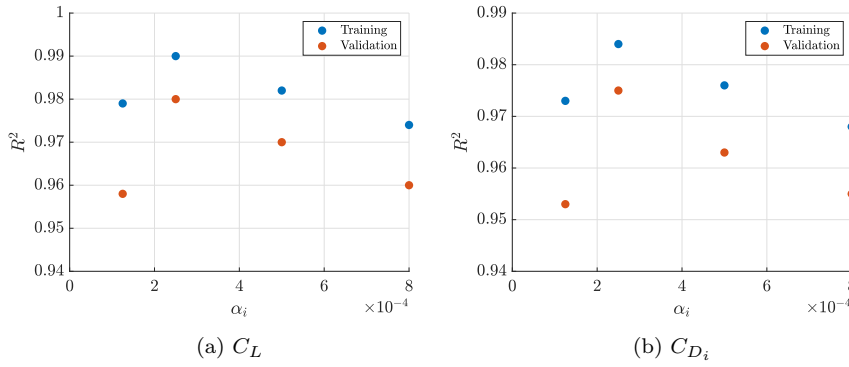
Fig. 6: Sensitivity to total number of kernels

The initial learning and the learning rate decay were also tuned to enable maximum training and validation accuracy with minimum possible training cost. Initial studies suggested 60,000 iterations to suffice. Thus, we select several initial learning rates α_i and adjusted our linear learning rate decay rate per iteration to reach the same final learning rate after 60,000 iterations. The results presented in Fig. 7 indicate that starting with $\alpha_i = 0.00025$ is optimal. Training with a higher initial rate leads to higher oscillations in the stochastic gradient descent and lower convergence. On the other hand, a slower initial learning rate leads to a slow convergence rate by the time 60,000 iterations have been completed. The C_L and C_{D_i} predicting networks with optimal hyperparameters were used subsequently for the optimization. The complete list of hyperparameters of the optimal network

Table 1: Hyperparameters of the optimally tuned CNN model

Hyperparameters	Values
Kernel size (δ)	4, 3, 3, 3
Number of kernels (n_k)	5, 10, 15, 20
Initial learning rate (α_i)	2.5e-4
Learn rate decay factor	0.999
Learn rate decay period	1 epoch
Epochs	3000
Batch size	750

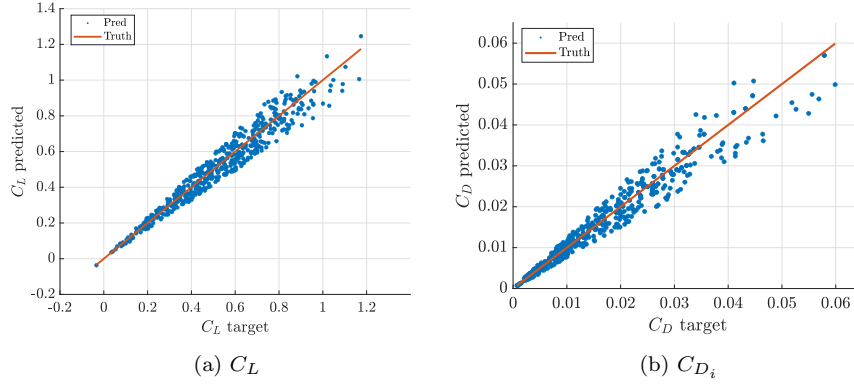
in shown below in Table 1. The kernel size and the number of kernels in each layer of the CNN model are shown.

Fig. 7: Sensitivity to α_i

We finally test our CNN on the test data set. The test data set will also serve as the initial starting designs for the subsequent gradient-based optimization study. The results presented in Fig. 8 (a) and (b) show the test predictions of the optimally tuned CNN network for the C_L and C_{D_i} , respectively. The lift coefficient predictions show reasonable agreement with the true results. The drag predictions show excellent agreement at low drag values and deviations from the true values are only observed for a few outliers at high values of the induced drag coefficient. Such high induced drag values will rarely be encountered when we optimize our designs to reduce induced drag and thus can be safely neglected for the present study. The predicted C_L and C_{D_i} have $R^2 = 0.94$ and $R^2 = 0.944$, respectively.

6.3 Deep CNN feature space exploration

We have shown earlier that the CNN can learn a functional relation between the shapes and their aerodynamic force coefficients. Here we will explore the feature maps of the kernels located in various layers of the deep CNN model to interpret the learning mechanism facilitated by the hierarchical deep CNN framework. We

Fig. 8: CNN test predictions for C_L and C_{D_i}

first present a representative wing and its corresponding level-sets in Figs. 9 (a) and (b), respectively. These will be used for generating the deep CNN feature maps.

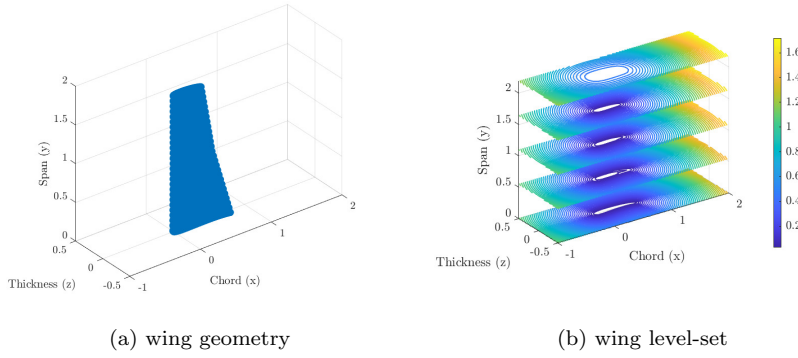


Fig. 9: Representative wing geometry and level-set

We first explore the feature maps of convolutional layer 1 of the network. Figs. 10 (a), (b) and (c) present the feature maps of the first, second and third kernels, respectively. Various slices are presented along the y axis of feature maps to show how they vary along the y -axis. Each slice shows the behavior of the feature maps along the $x - z$ plane at a specific y value. Fig. 10 (a) indicate that the first kernel focuses on the feature maps of the wing level-set (Fig. 9 (b)) lying near the upper boundary of the z axis. However, the weights for this kernel feature maps increase as move upward along the y axis (tip of the wing). The second kernel (Fig. 10 (b)) focuses on the input features lying near the center of the $x - z$ plane. The third kernel (Fig. 10 (c)) also focuses on the features near the center of the $x - z$ plane but more towards the lower limit of the y axis (root of the wing). These kernel feature maps are analogous to certain three-dimensional modes learnt by the

first convolutional layer as a result of a nonlinear decomposition of input level-set features into these kernels. However, unlike linear projection methods like POD, these CNN kernel feature maps are neither orthogonal in nature nor decomposed linearly.

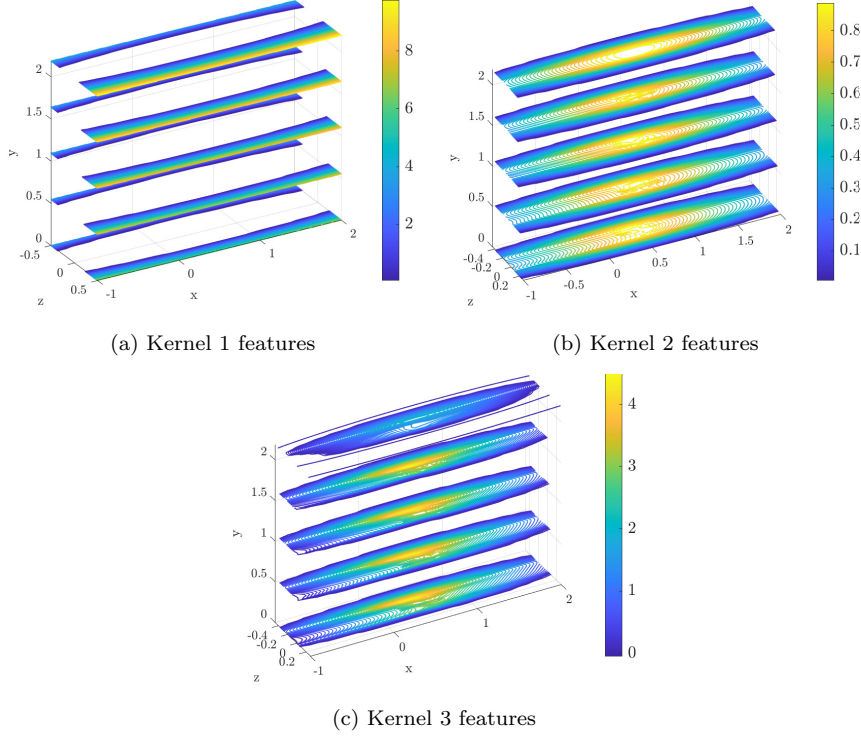


Fig. 10: Three-dimensional feature maps of first convolutional layer kernels

Similar to the first convolutional layer, we also investigate the features maps of various kernel outputs of the third convolutional layer. We specifically present the features of the 2nd, 7th and 14th kernel outputs of the third convolutional layer in Figs. 11 (a), (b) and (c), respectively. The 2nd kernel output shows a feature map whose $x - z$ features vary non-uniformly along the y -axis. The feature map (Fig. 11 (a)) focuses on the features near the center of the $x - z$ plane for lower values of y . It shows a uniform behavior along the $x - z$ plane near the middle of the y -axis and shows higher weights near the center of $x - z$ plane as y increases. Finally, near the upper limit of the y axis, the feature map weights along the $x - z$ plane progressively increases away from the center. For the 7th kernel, the feature maps (Fig. 11 (b)) focus specifically on the features close to the center of the $x - z$ and such output features show highest weight near the lower bound of the y axis. The output features becomes more uniformly distributed as we move up along the y axis. The 14th kernel output features (Fig. 11 (c)) focus on a specific level-set

isocurve on the $x - z$ axis. The feature are almost uniformly distributed along the y axis.

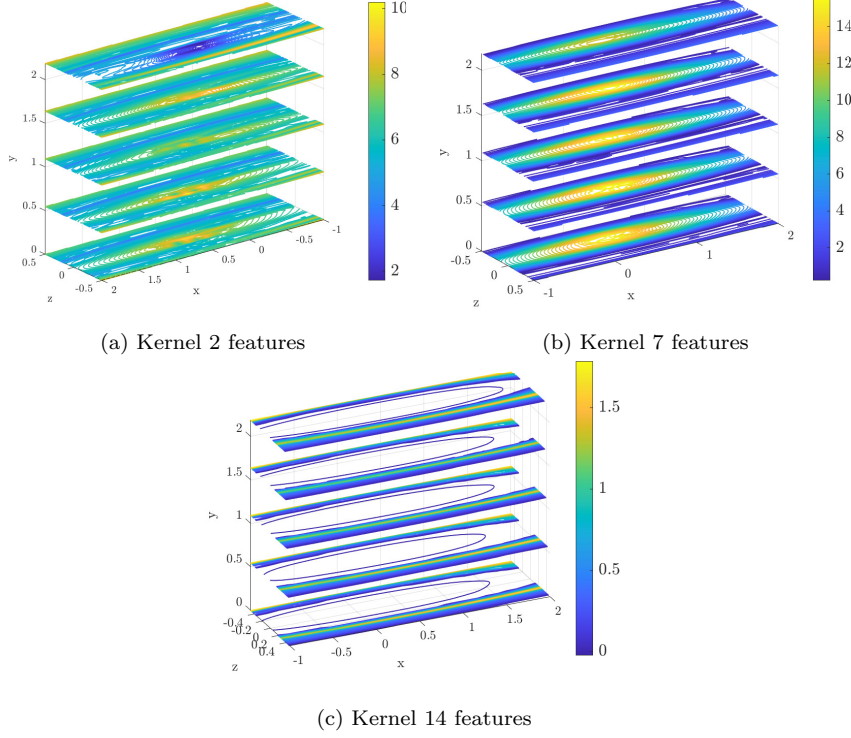


Fig. 11: 3D feature learning: third convolutional layer

Overall, we observe that the feature spaces of the various kernels of the third convolutional layer capture more localized features and show a more widely varying distribution along the various axes compared to their counterparts from the first convolutional layer. This can be explained by the fact that there are 15 kernels in the third layer compared to 5 in first layer. Thus, the nonlinear decomposition of the 10 kernel maps of the second convolutional layer outputs into the 15 kernel features of the third layer is a far more complex phenomena compared to a decomposition of the input level-sets to the 5 kernel feature maps of the first convolutional layer output. These kernel feature maps of the various convolutional layer provides physical insight into the learning mechanism of the CNN. The CNN's hierarchical structures enables a decomposition of input features into kernel feature maps, which becomes more complex and localized as we proceed deeper into the deep CNN framework, and eventually connects them to the aerodynamic force coefficients.

6.4 Gradient-based optimization results

We perform our gradient-based optimization by starting with several different initial design points. Such design space exploration is performed assuming the possibility for the objective function to show non-convex behavior in the thirty-three dimensional design space. Thus, 50 initial designs were selected randomly from the test set presented earlier and the optimization was performed for each of them with the DL-ROM. The constrained gradient-based optimization problem was solved using Sequential Quadratic Programming (SQP) algorithm from Matlab's *fmincon* function [46].

The objectives of the feasible designs are presented in Fig. 12. The final objective values of the feasible designs vary widely indicating the non-convex nature of the objective function, as suspected before. For all the feasible designs shown in Fig. 12, the objective functions were obtained with $R^2 = 0.94$ compared to their counterparts computed with the FOM. This demonstrates the accuracy of the CNN-based DL-ROM during the optimization process.

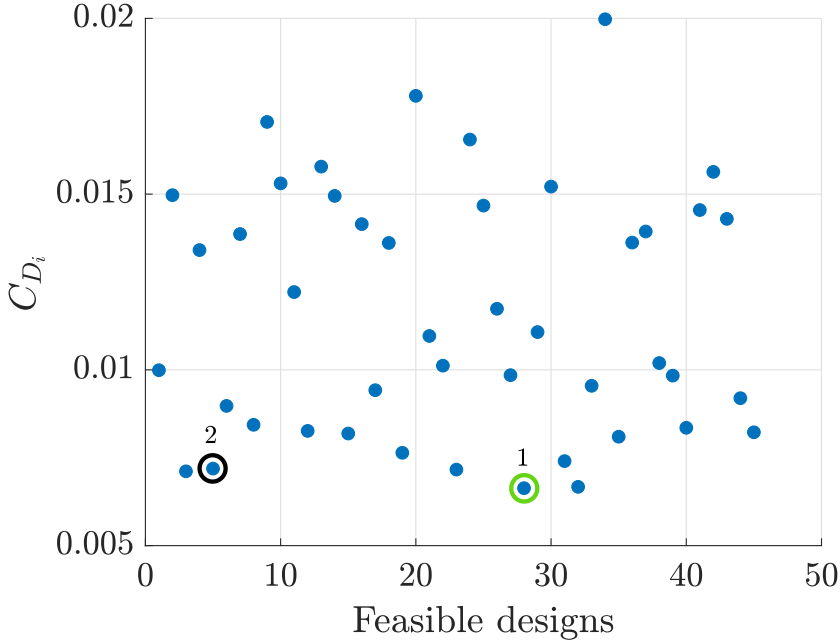


Fig. 12: Feasible designs

From these local optima, we select two designs 1 and 2, marked with circles in Fig. 12, for further inspection. Design 1 has an objective of $C_{D_i} = 0.0066$, which is minimum amongst all the feasible designs obtained. Design 2 has $C_{D_i} = 0.0072$, which is close to the best design obtained. The SQP optimization history for the optimal design 34 is presented in Fig. 13. The objective values first two iterations

of the gradient-based optimization as no feasible designs were obtained during those two iterations. This indicates the DL-ROM-based optimization was able to start from an infeasible design and was able to reach a local minimum significantly far away from the initial design.

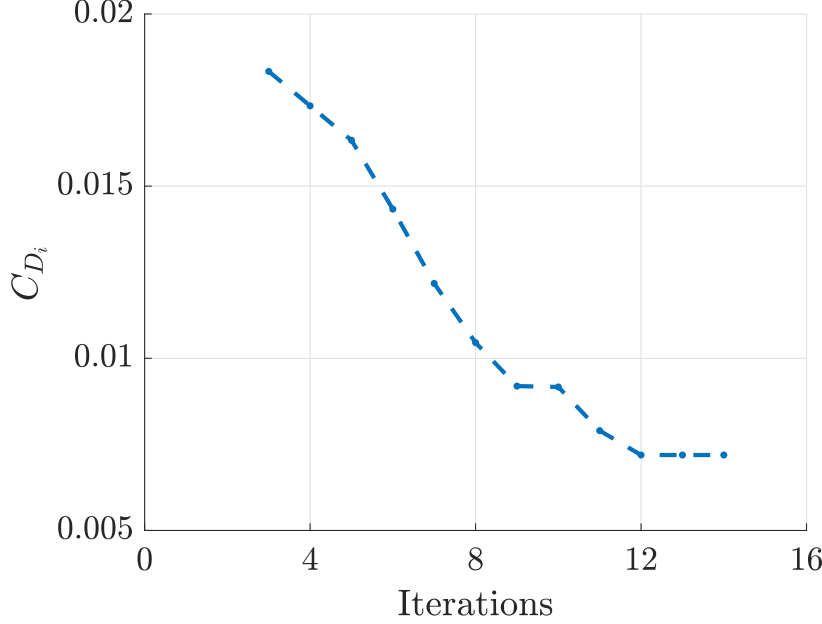


Fig. 13: SQP optimization convergence history

To further illustrate the differences between the initial and optimized designs, the wing sectional shapes were obtained at four different locations along the span: the root, 33%, and 67% of the span, and the wingtip, for design 2. These are shown in Figs. 14, 15, 16 and 17, respectively. We can observe that the optimization process significantly changed the wing's thickness distribution along the span. The thickness at the wing root increased, especially on the upper surface (Fig. 14). A significant increase in the wing section thickness is also observed at 33% of the span (Fig. 15). A small increase in the wing sectional thickness at 70-80% of the chord length on the lower surface is observed (Fig. 16) at 67% of the span. The inset showing a magnification is provided to illustrate this. No notable changes were observed at the wing root section. Apart from these changes in the wing sectional thickness, the wing's incident angle of attack also changed from 5.8 degrees to 4.9 degrees due to the optimization process. These changes first ensured that the wing satisfies the thickness and the C_L constraints as shown in Fig. 13, and then the induced drag reached a local minimum.

The lifting line theory can be theoretically employed to show that for minimum induced drag for a specific configuration, the required lift distribution for the wing should be elliptic in nature. Thus, such lift distribution is an indicator

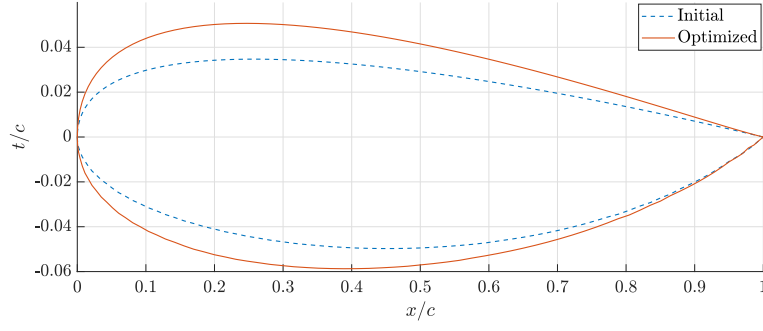


Fig. 14: Comparison of initial and optimized wing sections: root

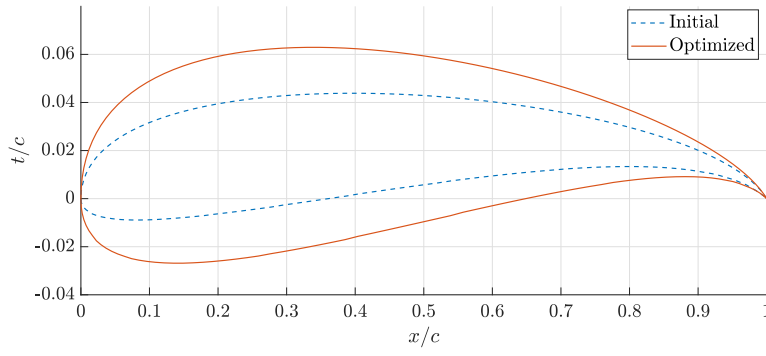


Fig. 15: Comparison of initial and optimized wing sections: 33% span

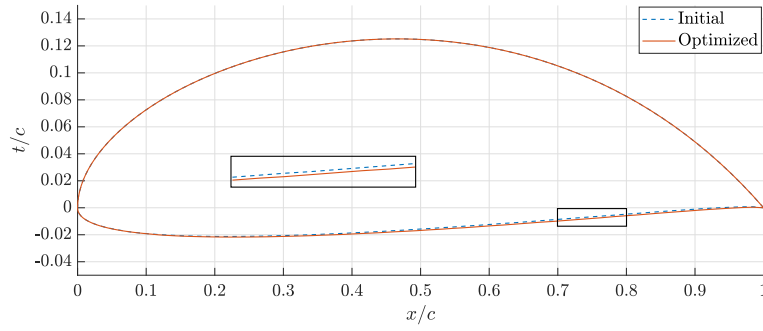


Fig. 16: Comparison of initial and optimized wing sections: 67% span

of the theoretical optimality of the configuration. We calculate the wing lift distribution for the initial and final configurations for design 2 to compare the effects of the DL-ROM-based optimization. The computed lift distribution compared to an elliptic lift distribution is shown in Figs. 18 (a) and (b), for the initial and

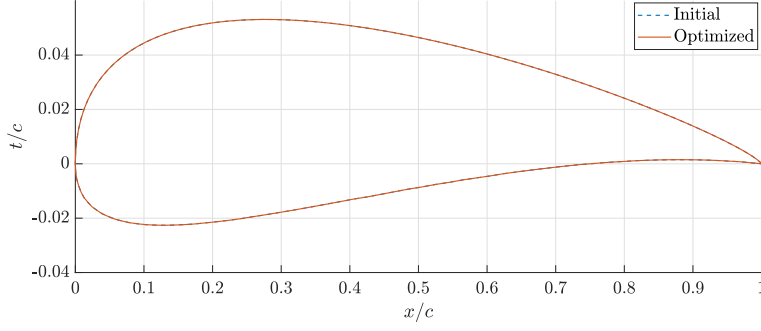
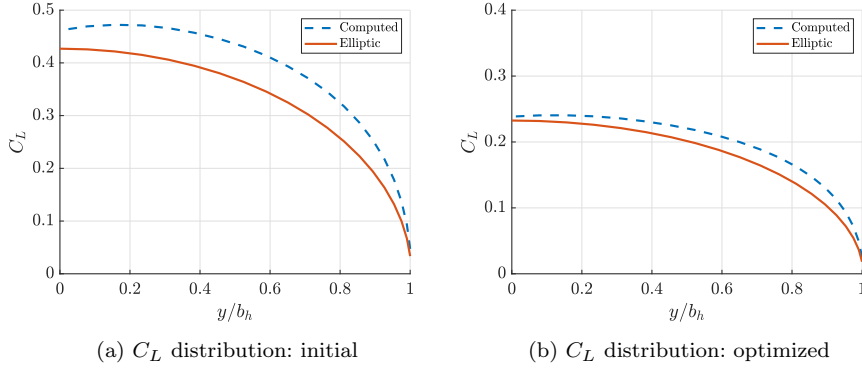


Fig. 17: Comparison of initial and optimized wing sections: tip

optimized designs, respectively. We can see that the initial design 2 not only violates certain constraints, but its lift distribution is far away from the optimal elliptic distribution, especially at the wing root. For the final design obtained via the DL-ROM-based optimization, the lift distribution does not exactly match the elliptic lift distribution but is much closer to it as a result of the optimization. To further understand the source of this difference in the optimized lift distribution, we perform a similar comparison for the optimized design 1. Since the optimized design 1 has a lower C_{D_i} than optimized design 2, we can expect a better match with the theoretical prediction for a global optimum. Fig 19 shows that the lift distribution of the optimized design 1 matches the elliptic lift distribution almost exactly near the wingtip. Some small differences are observed near the wing root. Overall, it follows the theoretically predicted optimum much better than design 2. This shows that DL-ROM-based optimization was able to provide physically consistent results over a range of design values.

Fig. 18: C_L distribution of design 2

The small differences between the theoretical and actual optimized solutions for design 1 could be a consequence of several factors. It could arise from the assump-

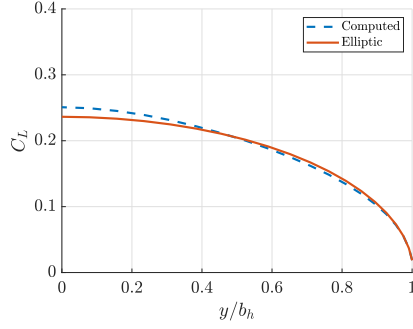


Fig. 19: Optimized C_L distribution of design 1

tions considered in the development of the DL-ROM ranging from implicit shape approximation via level-sets to the FOM approximation via CNNs. However, it is also possible that the exploration of the design space with gradient-based optimization could not lead to the true global minimum. Thus, future shape optimization research would consider the application of metaheuristic global optimization algorithms [37] or a multi-fidelity analysis with trust region-based algorithm [27], both of which offer more robustness than gradient-based methods.

6.5 Computational efficiency

The total cost of training the CNN model was 11 hours on a single NVIDIA v100 Tensor Core GPU. The prediction phase for the CNN model includes the generation of the distance function from the airfoil shape parameters and subsequent CNN-based computation. This requires roughly 30 CPU seconds. The SQP-based gradient optimization with the CNN-based DL-ROM required roughly 500 CPU seconds on average. Since the CNN-based optimization is a completely data-driven process, its total computation time is independent of the fidelity of the computational solver or the experimental process employed. The reported computational time associated with two-dimensional RANS-based optimization [5] and direct numerical simulations of two-dimensional Navier-Stokes equations [31] indicate that the DL-ROM can provide significant computational efficiency during online applications even for two-dimensional cases. For the three-dimensional cases shown here, the reduction in computational time can be expected to increase many folds, especially as the number of design points increases. However, the exact magnitude of the reduction in computational cost cannot be reported at this point to the lack of computational cost reported for three-dimensional shape-optimizations with high-fidelity computational solvers.

7 Conclusions

This article presents a novel deep learning-based model order reduction methodology for shape optimization applications via a deep convolutional neural network (CNN) and a level-set shape representation. The CNN provides a nonlinear

mapping between the shapes and their associated features while conserving the equivariance of these features to the shape translations. Such a mapping can be achieved via the CNN with sufficient accuracy but at an improved computational efficiency compared to high-fidelity full-order models (FOM). CNNs require input data in a structured Cartesian grid. To provide an implicit representation of complex three-dimensional shapes on a uniform structured grid, level-set methods were employed. The level-set representation not only enables the generic application of CNN models but also provides coarse-graining when the explicit representation of the shapes requires many parameters and is not computationally efficient for optimization applications.

The CNN model is obtained in a completely data-driven manner. This makes it applicable as a reduced-order model (ROM) to the FOM for a wide range of physical problems, irrespective of how the physical data is acquired. Furthermore, the deep learning-based ROM (DL-ROM) can be applied non-intrusively during optimization, thus enabling seamless integration to any general gradient-based or metaheuristic optimization algorithms.

We demonstrate our complete DL-ROM-based optimization methodology by integrating it to an optimization algorithm employed for minimizing the induced drag of a wing in three-dimensional potential flow. We demonstrate satisfactory training, validation and test performance of our deep CNN model by optimal hyperparameter tuning. We also show a reasonably accurate comparison between the aerodynamic coefficient of our optimized solutions to those obtained from a potential flow solver used for generating the three-dimensional training data sets. Furthermore, we demonstrate the physically consistent nature of our DL-ROM-based optimization by demonstrating a close match between the optimal design lift distribution obtained via the DL-ROM to the elliptic lift distribution predicted for a theoretical optimum. We also provide interpretability to the learning mechanism of the deep CNN model by exploring the kernel feature maps of the various convolutional layers of our deep CNN model.

The CNN-based shape optimization algorithm demonstrates computational efficiency during online optimization applications and promises a tractable solution for performing shape optimization for any general three-dimensional shape optimization problem. In the future, we plan to employ the DL-ROM-based optimization methodology to more physically complex and larger-scale problems, where training data will be obtained from high-fidelity computational solvers or experiments. We also plan to our deep learning-based ROM as part of a multi-fidelity analysis model in future with various gradient-free optimization techniques.

Acknowledgments

This research was supported by the Natural Sciences and Engineering Research Council of Canada (NSERC) [grant number IRCPJ 550069-19]. The second author would like to thank the financial support from the NSERC Undergraduate Student Research Award. We would also like to acknowledge that the GPU facilities at the Compute Canada clusters were used for the training of our deep convolutional neural network models.

Table 2: n_k distribution in each layer of the CNN models

Total number of kernels	Kernel distribution	Total trainable parameters
22	4, 5, 6, 7	7829
28	4, 6, 8, 10	21365
43	5, 9, 13, 16	86973
46	5, 10, 14, 17	110646
50	5, 10, 15, 20	139451
56	6, 11, 16, 21	206164

Conflict of interest

The authors declare that they have no conflict of interest.

Appendix

CNN hyperparameter tuning

The distribution of the kernels in each layer of the various CNN models presented in Fig. 6 are presented in Table 2. The model size for each of these CNN model is indicated by the total trainable parameters available for each model.

References

1. Allaire, G., Jouve, F., Toader, A.M.: Structural optimization using sensitivity analysis and a level-set method. *Journal of computational physics* **194**(1), 363–393 (2004)
2. Blatman, G.: Adaptive sparse polynomial chaos expansions for uncertainty propagation and sensitivity analysis. Ph.D. thesis, Clermont-Ferrand 2 (2009)
3. Bonfiglio, L., Perdikaris, P., Vernengo, G., de Medeiros, J.S., Karniadakis, G.: Improving swath seakeeping performance using multi-fidelity gaussian process and bayesian optimization. *Journal of Ship Research* **62**(04), 223–240 (2018)
4. Bouhlel, M.A., Bartoli, N., Otsmane, A., Morlier, J.: Improving kriging surrogates of high-dimensional design models by partial least squares dimension reduction. *Structural and Multidisciplinary Optimization* **53**(5), 935–952 (2016)
5. Bouhlel, M.A., He, S., Martins, J.R.: Scalable gradient-enhanced artificial neural networks for airfoil shape design in the subsonic and transonic regimes. *Structural and Multidisciplinary Optimization* pp. 1–14 (2020)
6. Bronstein, M.M., Bruna, J., LeCun, Y., Szlam, A., Vandergheynst, P.: Geometric deep learning: going beyond euclidean data. *IEEE Signal Processing Magazine* **34**(4), 18–42 (2017)
7. Chernukhin, O., Zingg, D.W.: Multimodality and global optimization in aerodynamic design. *AIAA journal* **51**(6), 1342–1354 (2013)
8. Cybenko, G.: Approximation by superpositions of a sigmoidal function. *Mathematics of control, signals and systems* **2**(4), 303–314 (1989)
9. Fan, X., Wang, P., Hao, F.: Reliability-based design optimization of crane bridges using kriging-based surrogate models. *Structural and Multidisciplinary Optimization* **59**(3), 993–1005 (2019)
10. Feng, Y., Chen, Z., Dai, Y., Wang, F., Cai, J., Shen, Z.: Multidisciplinary optimization of an offshore aquaculture vessel hull form based on the support vector regression surrogate model. *Ocean Engineering* **166**, 145–158 (2018)
11. Garg, N., Kenway, G.K., Lyu, Z., Martins, J.R., Young, Y.L.: High-fidelity hydrodynamic shape optimization of a 3-d hydrofoil. *Journal of Ship Research* **59**(4), 209–226 (2015)

12. Goodfellow, I., Bengio, Y., Courville, A.: Deep learning. MIT press (2016)
13. Haftka, R.T., Grandhi, R.V.: Structural shape optimization—a survey. *Computer methods in applied mechanics and engineering* **57**(1), 91–106 (1986)
14. Han, Z.H., Abu-Zurayk, M., Görtz, S., Ilic, C.: Surrogate-based aerodynamic shape optimization of a wing-body transport aircraft configuration. In: *Symposium on AeroStructures*, pp. 257–282. Springer (2015)
15. He, X., Li, J., Mader, C.A., Yildirim, A., Martins, J.R.: Robust aerodynamic shape optimization—from a circle to an airfoil. *Aerospace Science and Technology* **87**, 48–61 (2019)
16. Hornik, K.: Approximation capabilities of multilayer feedforward networks. *Neural networks* **4**(2), 251–257 (1991)
17. Ioffe, S., Szegedy, C.: Batch normalization: Accelerating deep network training by reducing internal covariate shift. In: *International conference on machine learning*, pp. 448–456. PMLR (2015)
18. Kapania, R.K., Schetz, J.A., Mallik, W., Segee, M.C., Gupta, R.: Multidisciplinary design optimization and cruise mach number study of truss-braced wing aircraft. Tech. rep., NASA/CR-2018-219836, NF1676L-27943 (2018)
19. Keane, A., Forrester, A., Sobester, A.: Engineering design via surrogate modelling: a practical guide. American Institute of Aeronautics and Astronautics, Inc. (2008)
20. Kingma, D.P., Ba, J.: Adam: A method for stochastic optimization. *arXiv preprint arXiv:1412.6980* (2014)
21. Koziel, S., Leifsson, L.: Surrogate-based aerodynamic shape optimization by variable-resolution models. *AIAA journal* **51**(1), 94–106 (2013)
22. Krige, D.G.: A statistical approach to some basic mine valuation problems on the witwatersrand. *Journal of the Southern African Institute of Mining and Metallurgy* **52**(6), 119–139 (1951)
23. LeCun, Y., Bengio, Y., Hinton, G.: Deep learning. *Nature* **521**(7553), 436–444 (2015)
24. Lyu, Z., Kenway, G.K., Martins, J.R.: Aerodynamic shape optimization investigations of the common research model wing benchmark. *AIAA journal* **53**(4), 968–985 (2015)
25. Maas, A.L., Hannun, A.Y., Ng, A.Y.: Rectifier nonlinearities improve neural network acoustic models. In: *Proc. icml*, vol. 30, p. 3. Citeseer (2013)
26. Mallik, W., Raveh, D.E.: Kriging-based aeroelastic gust response analysis at high angles of attack. *AIAA Journal* **58**(9), 3777–3787 (2020)
27. Marques, S.P., Kob, L., Robinson, T.T., Yao, W., Sun, L.: Non-intrusive aerodynamic shape optimisation with a discrete empirical interpolation method. In: *AIAA Scitech 2021 Forum*, p. 0172 (2021)
28. Martins, J.R., Hwang, J.T.: Review and unification of methods for computing derivatives of multidisciplinary computational models. *AIAA journal* **51**(11), 2582–2599 (2013)
29. Matthews, A.G.d.G., Rowland, M., Hron, J., Turner, R.E., Ghahramani, Z.: Gaussian process behaviour in wide deep neural networks. *arXiv preprint arXiv:1804.11271* (2018)
30. Miyanawala, T., Jaiman, R.K.: A novel deep learning method for the predictions of current forces on bluff bodies. In: *International Conference on Offshore Mechanics and Arctic Engineering*, vol. 51210, p. V002T08A003. American Society of Mechanical Engineers (2018)
31. Miyanawala, T.P., Jaiman, R.K.: An efficient deep learning technique for the navier-stokes equations: Application to unsteady wake flow dynamics. *arXiv preprint arXiv:1710.09099* (2017)
32. Mojjani, R., Balajewicz, M.: Low-rank registration based manifolds for convection-dominated pdes. In: *Proceedings of the AAAI Conference on Artificial Intelligence*, vol. 35, pp. 399–407 (2021)
33. Nagawkar, J.R., Leifsson, L.T., He, P.: Aerodynamic shape optimization using gradient-enhanced multifidelity neural networks. In: *AIAA SCITECH 2022 Forum*, p. 2350 (2022)
34. Perdikaris, P., Raissi, M., Damianou, A., Lawrence, N.D., Karniadakis, G.E.: Nonlinear information fusion algorithms for data-efficient multi-fidelity modelling. *Proceedings of the Royal Society A: Mathematical, Physical and Engineering Sciences* **473**(2198), 20160751 (2017)
35. Raissi, M., Karniadakis, G.: Deep multi-fidelity gaussian processes. *arXiv preprint arXiv:1604.07484* (2016)
36. Reuther, J., Jameson, A., Farmer, J., Martinelli, L., Saunders, D.: Aerodynamic shape optimization of complex aircraft configurations via an adjoint formulation. In: *34th Aerospace Sciences Meeting and Exhibit*, p. 94 (1996)
37. Samanipour, F., Jelovica, J.: Adaptive repair method for constraint handling in multi-objective genetic algorithm based on relationship between constraints and variables. *Applied Soft Computing* **90**, 106143 (2020)

38. Samareh, J.: Aerodynamic shape optimization based on free-form deformation. In: 10th AIAA/ISSMO multidisciplinary analysis and optimization conference, p. 4630 (2004)
39. Schobi, R., Sudret, B., Wiart, J.: Polynomial-chaos-based kriging. *International Journal for Uncertainty Quantification* **5**(2) (2015)
40. Sethian, J.A.: Theory, algorithms, and applications of level set methods for propagating interfaces. *Acta numerica* **5**, 309–395 (1996)
41. Singh, K., Kapania, R.K.: Alga: Active learning-based genetic algorithm for accelerating structural optimization. *AIAA Journal* **59**(1), 330–344 (2021)
42. Sóbester, A., Barrett, T.: Quest for a truly parsimonious airfoil parameterization scheme. In: The 26th Congress of ICAS and 8th AIAA ATIO, p. 8879 (2008)
43. Sóbester, A., Forrester, A.I.: *Aircraft aerodynamic design: geometry and optimization*. John Wiley & Sons (2014)
44. Streuber, G.M., Zingg, D.W.: Evaluating the risk of local optima in aerodynamic shape optimization. *AIAA Journal* pp. 1–13 (2020)
45. The MathWorks, I.: Matlab deep learning toolbox. URL <https://www.mathworks.com/help/deeplearning/>
46. The MathWorks, I.: Matlab optimization toolbox. URL <https://www.mathworks.com/help/optim/>
47. Timme, S., Marques, S., Badcock, K.: Transonic aeroelastic stability analysis using a kriging-based schur complement formulation. *AIAA journal* **49**(6), 1202–1213 (2011)
48. Wang, S., Lim, K.M., Khoo, B.C., Wang, M.Y.: An extended level set method for shape and topology optimization. *Journal of Computational Physics* **221**(1), 395–421 (2007)
49. Wang, S., Sun, G., Chen, W., Zhong, Y.: Database self-expansion based on artificial neural network: An approach in aircraft design. *Aerospace Science and Technology* **72**, 77–83 (2018)
50. Wang, S., Wang, M.Y.: Radial basis functions and level set method for structural topology optimization. *International journal for numerical methods in engineering* **65**(12), 2060–2090 (2006)
51. Yao, W., Marques, S., Robinson, T., Armstrong, C., Sun, L.: A reduced-order model for gradient-based aerodynamic shape optimisation. *Aerospace Science and Technology* **106**, 106120 (2020)
52. Yondo, R., Andrés, E., Valero, E.: A review on design of experiments and surrogate models in aircraft real-time and many-query aerodynamic analyses. *Progress in aerospace sciences* **96**, 23–61 (2018)